Brillouin and dielectric sidescatter of 10-μm light by a plasma

Mark J. Herbst,[a] Christopher E. Clayton, and Francis F. Chen
Electrical Sciences and Engineering Department, University of California, Los Angeles, California 90024

(Received 20 February 1980; accepted for publication 19 March 1980)

Sidescatter of CO_2 laser light from underdense, laser-heated plasmas in H_2 and He is observed at $\theta = 90°$. Spectrum, exponentiation, isotropy, and polarization measurements are used to deconvolve two separate mechanisms: (1) Doppler-shifted reflections from moving dielectric discontinuities created in the laser-ionization process, and (2) Stimulated Brillouin scattering seeded by these reflections. The dielectric sidescatter is unpolarized and azimuthally symmetric, similar to the diffuse component of scattering in solid-target experiments. The Brillouin sidescatter saturates at a low level corresponding to an ion wave amplitude of 0.1–1.0%, consistent with previous data on the saturation of backscatter.

PACS numbers: 52.35.Py, 52.40.Db, 52.25.Ps

I. INTRODUCTION

Stimulated Brillouin scattering (SBS)[1] at 180° has been the subject of numerous experimental studies with both solid and gaseous plasma targets,[2] because this process can adversely affect the absorption efficiency in laser-pellet fusion tests with long pulses and ablative pushers. Brillouin *sidescatter*, on the other hand, has received relatively little attention, even though the theoretical growth rate is comparable to that for backscatter. In solid-target sidescatter experiments,[3–9] the presence of a critical layer complicates the observations; in only one of these[8] is a sidescattered spectrum obtained, and no identification of SBS is made. In many cases, sidescatter is found to be independent of the plane of polarization, a result not expected for either SBS or classical reflection from a smooth surface.

In the present work, we have studied sidescatter in a plasma that is everywhere underdense, thus simplifying the interpretation of the results. Clear evidence of SBS sidescatter is found for the first time. In addition, sidescatter due to a second mechanism, dielectric reflection, is also observed. The latter may throw light on the diffuse scatter, inconsistent with SBS, found in some solid-target experiments.[9]

II. EXPERIMENTAL APPARATUS

Figure 1 shows the experimental arrangement, which has been described previously.[10] Thirty joules (300 MW) of gain-switched multimode output from a CO_2 oscillator-amplifier chain is extracted in a linearly polarized, 10-cm-diam annular beam. With a 75.5-cm focal length antireflection coated germanium lens, this beam is focused into hydrogen or helium gas preionized by a pulsed arc discharge. The lens used is of better quality than that used in Ref. 10; a focal spot diameter of $280 \pm 30\,\mu$m at the half-power points results in a vacuum intensity $I_0 \simeq 5 \times 10^{11}$ W/cm^2. The position of the CO_2 focal spot relative to the arc plasma also differs from that used previously; the focus is located at the center of the column, at a position corresponding to the sidescatter collection volume.

Two plasmas are used: 15.2-Torr hydrogen gas preionized to $n_e \simeq 1 \times 10^{16}$ cm^{-3}, and 25-Torr helium gas preionized to $n_e \simeq 3 \times 10^{15}$ cm^{-3}. Pressures are chosen to be below the laser-induced gas breakdown threshold in the absence of arc preionization, but greater than the threshold for sidescatter detection. As both of these limits are higher in helium than in hydrogen, a higher operating pressure is used in helium. Near the focus, of course, ionization and heating by the laser lead to significantly different plasma parameters than are observed in the arc.

Sidescattered light is collected from the center of the arc by an $f/5$ lens and directed to an infrared detection system consisting of two liquid-helium cooled, doped-germanium photoconductors. One detector sits behind a Fabry-Perot

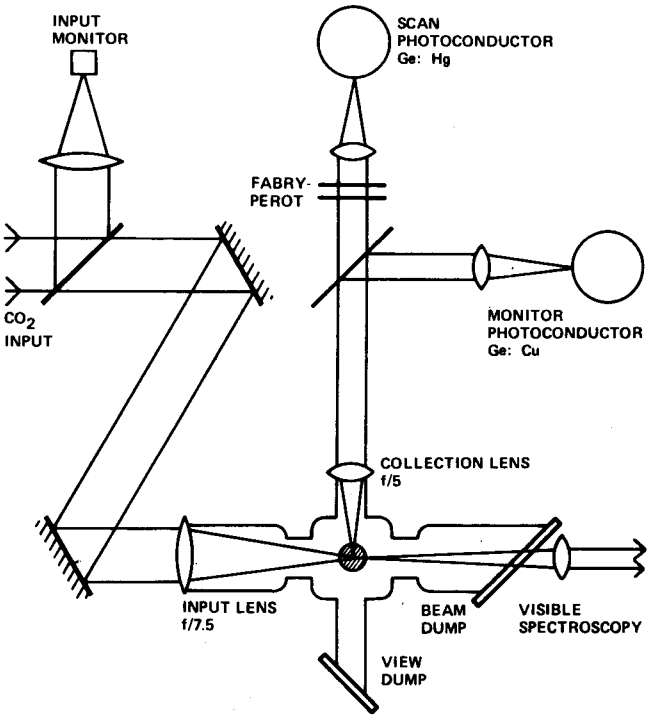

FIG. 1. Schematic of experimental arrangement used for study of sidescatter.

[a]Present address: Naval Research Laboratory, Washington D.C. 20375

 0021-8979/80/084080-08$01.10

interferometer, which may be piezoelectrically scanned between shots to generate spectra of scattered light. The second detector serves as a monitor of total scattered light, so that shot-to-shot variations in that quantity may be normalized out of the spectral data. To measure polarization of sidescattered light, a stack of germanium plates is used.

Plasma diagnosis, as described in Ref. 10, was done primarily by ruby laser holographic interferometry and by visible spectroscopy. The axis used for interferometric measurements is the same as that usually used for sidescatter collection. Visible line and continuum emission from the plasma is collected along the input laser axis through the Plexiglass beam dump. Spectra are obtained using a 2-m spectrograph and Optical multichannel analyzer (OMA). Time resolution of the interferometry and spectroscopy is limited by the 30-ns (FWHM) ruby laser pulse width and 40-ns (FWHM) electrical OMA gate, respectively.

III. RESULTS

Stimulated Brillouin sidescatter is always expected to have the following two properties. First, the spectrum of the scattered light is red shifted from the incident laser frequency by the frequency of an acoustic wave propagating at 45° to the incident direction. In an underdense plasma, the shift is therefore $\sqrt{2}$ smaller than in backscatter. Second, the sidescatter reflectivity, defined as the ratio between scattered power and incident power, should increase with input power. In other words, the scattered power is not proportional to input power, as it would be for a linear process such as thermal Thomson scattering.

For linearly polarized input beams with weak focusing (small angles of convergence), two additional properties are expected of SBS sidescatter. There should be anisotropy of sidescattered power in the plane orthogonal to the incident wave vector. Scattering should occur preferentially in a direction normal to the plane of polarization of the incident beam ($\phi = 90°$), and should be small in a direction parallel to the incident electric vector $\mathbf{E}_0(\phi = 0°)$. In addition, the sidescattered light should itself be linearly polarized. In examining the data, one relies on these expected features to distinguish between SBS and other processes.

A. Sidescatter observations in hydrogen

The relative time histories of hydrogen sidescatter and input laser pulses are shown in Fig. 2. From Fig. 2(a) it may be seen that sidescatter is of short duration and occurs near

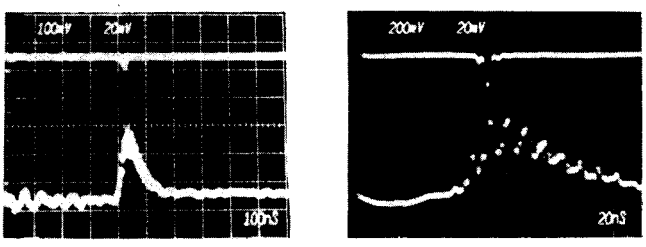

(a) (b)

FIG. 2. Time history of hydrogen sidescatter (upper traces) relative to input laser pulse (lower traces) on: (a) 100 nsec/div and (b) 20 nsec/div.

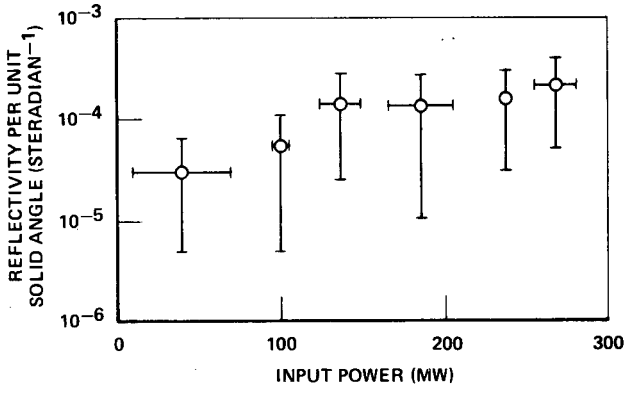

FIG. 3. Variation of hydrogen sidescatter reflectivity per unit solid angle with input power. Error bars represent standard deviation of at least ten shots. Reflectivity is defined as peak scattered power divided by input power at the time of scattering; this peak power reflectivity in these long-pulse experiments roughly corresponds to energy reflectivities in short-pulse experiments.

the time of the peak of the CO_2 input. The very fast turn-on and turn-off reminiscent of SBS backscatter from this device[2] is even more evident in Fig. 2(b).

The sidescatter reflectivity per unit solid angle is found to vary with input power as shown in Fig. 3. Some increase of reflectivity with input power is suggested by the plot, though the large error bars would just allow a constant reflectivity curve to pass through the points. Each point represents an average over ten or more shots; the error bars reflect shot-to-shot variations in reflectivity, which are much larger than errors due to other sources.

Since the input beam is linearly polarized and the range of incident ray angles due to the long input lens focal length is small, anisotropy of sidescattered power in the plane perpendicular to the incident wave vector $\mathbf{k}_0$ is expected [see Fig. 4(a)]. Using the axis through the hollow electrodes of the arc discharge as a second sidescatter collection axis, simultaneous observations of sidescatter at $\phi = 0°$ and $\phi = 90°$ are made. Experimental geometry forces use of an $f/15$ sidescatter collection lens along this second axis; to be certain that differences in observed sidescatter properties are caused by the difference in ϕ and not by geometrical effects, input beam polarization is rotated by 90° so that sidescatter at both $\phi = 0°$ and $\phi = 90°$ is observed using both axes. It is found that the ratio of the sidescattered power at $\phi = 90°$ to that at $\phi = 0°$ varies from shot to shot between $\frac{1}{3}$ and 3; the average over many shots is 1.1, but with a large error bar corresponding to the shot-to-shot variation.

Investigating the apparent isotropy of this sidescatter further, we measured the spectra of light sidescattered at $\phi = 90°$ and $\phi = 0°$. At $\phi = 0°$, as seen from Fig. 4(b), a broad spectrum centered about 12 GHz to the red of the incident frequency is observed. The dominant feature of the spectrum at $\phi = 90°$, shown in Fig. 4(c), is a peak shifted between 12.5 and 15.0 GHz to the red. This shift is approximately $\sqrt{2}$ less than the 21–23 GHz shift observed for hydrogen SBS backscatter,[2] though the sidescatter and backscatter source regions in the plasma are different.[10] A second feature, a shelf extending into the blue, is also observed in this spectrum.

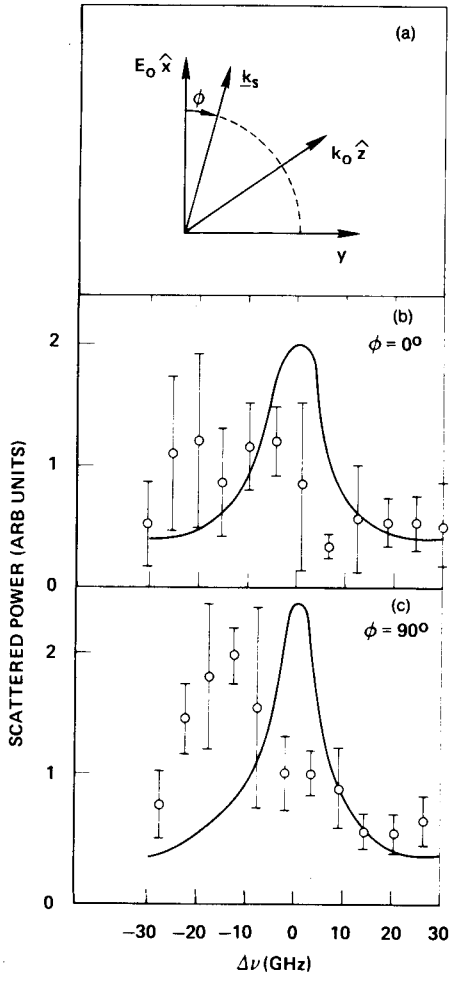

FIG. 4. (a) Geometry of sidescatter experiment, showing the wave vector $\mathbf{k}_0$ and electric field vector $\mathbf{E}_0$ of the linearly polarized input beam along the z and x axes, respectively. Angle ϕ specifies orientation of sidescattered wave vector $\mathbf{k}_s$ relative to $\mathbf{E}_0$ in the x-y plane. Not shown is the polar angle θ between $\mathbf{k}_0$ and $\mathbf{k}_s$; only the case $\theta = 90°$ is treated in this paper. (b) Spectrum of sidescatter at $\phi = 0°$ (points) is compared with the measured interferometer instrument function centered at the frequency of the incident laser (curve). (c) Same as (b), but for $\phi = 90°$.

In light of the above-mentioned isotropy, a measurement of the polarization of sidescattered light is also made. For the linearly polarized input with weak focusing, one expects scattered light at $\phi = 90°$ to be linearly polarized with electric field vector $\mathbf{E}_s$ parallel to $\mathbf{E}_0$. Using a polarization analyzer consisting of four germanium plates canted at the Brewster angle and the two infrared detectors previously described, we measured the ratio of the scattered power transmitted by the polarizer to the total scattered power on each shot. Comparing the average ratios measured with the polarizer transmitting in each direction (on different shots), we found that average scattered power with $\mathbf{E}_s \| \mathbf{E}_0$ is 1.3 times the average scattered power with $\mathbf{E}_s \perp \mathbf{E}_0$. However, the error bar due to shot-to-shot variation encompasses the range between 0.4 and 4.5. Even the upper extreme of this range corresponds to considerable depolarization; for the ratio is a factor of 4 less than observed for the incident beam at the entrance to the arc vacuum vessel. To test whether the

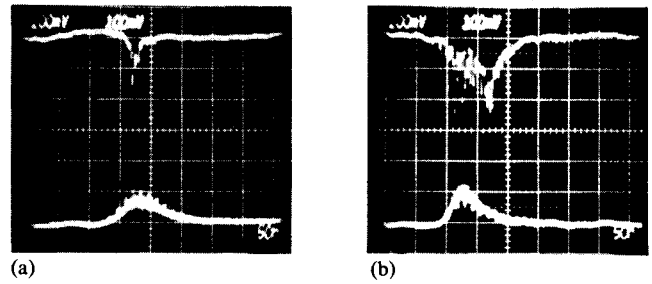

FIG. 5. Time histories of helium sidescatter (upper traces) relative to input laser pulse (lower traces) on 50 nsec/div for (a) single-spike sidescatter and (b) multiple-spike sidescatter.

measured depolarization could merely be the effect of focusing, a crudely polished piece of aluminum is aligned at the focal spot of the incident beam (suitably attenuated to prevent plasma formation at the surface) so as to reflect into the sidescatter collection optics. A ratio of 9 ± 4 is measured between sidescatter with $\mathbf{E}_s \| \mathbf{E}_0$ and sidescatter with $\mathbf{E}_s \perp \mathbf{E}_0$, indicating that focusing geometry is not responsible for the depolarization of light scattered by the plasma.

B. Sidescatter observations in helium

Two types of sidescatter time histories are observed with helium plamas. Single-spike sidescatter, shown in Fig. 5(a), occurs in a single narrow pulse near the time of peak

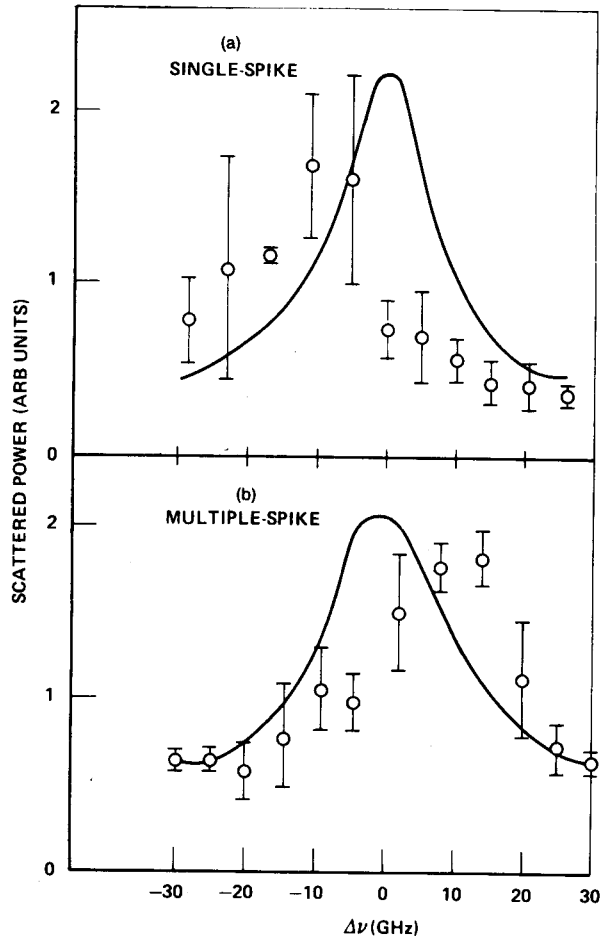

FIG. 6. Spectra of (a) single-spike and (b) multiple-spike helium sidescatter at $\phi = 90°$.

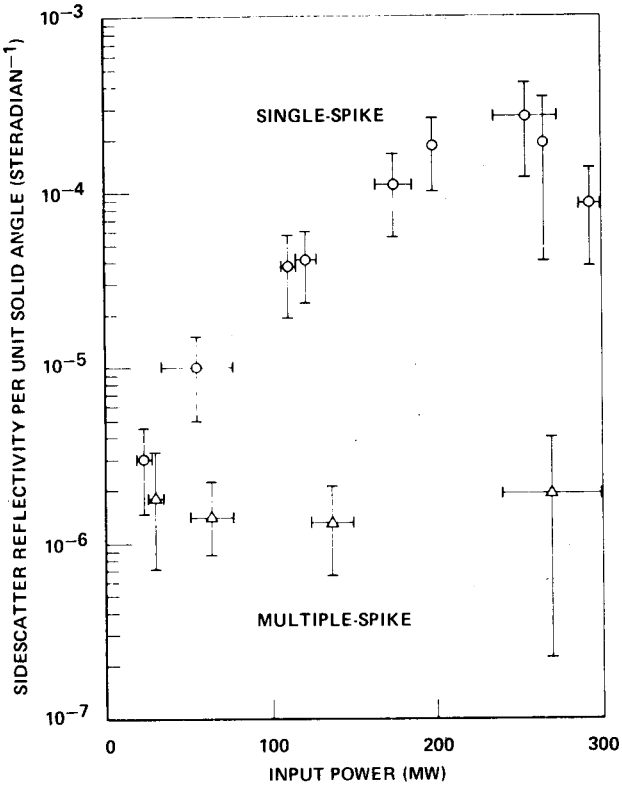

FIG. 7. Variation of single-spike (○) and multiple-spike (△) sidescatter reflectivities per unit solid angle with input power.

CO_2 input; this type of sidescatter occurs only if the laser is fired during a narrow window in time relative to the preionization pulse. The full reason for this sensitivity to relative timing is not understood, though similar observations in hydrogen have been explained in terms of the dependence of the plasma evolution upon the preionization level.[10] Outside this window, the sidescatter signature is as shown in Fig. 5(b); while still spiky, the duration of this multiple-spike scattering is much longer.

Different spectra are obtained for these two kinds of sidescatter, as indicated in Fig. 6 for $\phi = 90°$. The single-spike sidescatter spectrum in Fig. 6(a) has a single peak, red shifted by 7.5–10 GHz. The multiple-spike sidescatter spectrum in Fig. 6(b) is broad, with a peak shifted 10–12.5 GHz to the blue.

The variation of reflectivity per unit solid angle with input power for single- and multiple-spike sidescatter is shown in Fig. 7. Whereas an approximately constant reflectivity is seen for multiple-spike sidescatter, single-spike sidescatter reflectivity initially grows with input power and then apparently saturates. Note that at the lowest input powers the levels of the two kinds of sidescatter appear to merge.

Measurements of sidescatter anisotropy and polarization are also made. At $\phi = 0°$, sidescatter is observed to have only the broad, blue-weighted spectrum and constant reflectivity that is characteristic of multiple-spike sidescatter at $\phi = 90°$. The time history of this sidescatter, however, is shorter in duration than multiple-spike sidescatter. Polarization measurements of sidescatter at $\phi = 90°$ reveal that the ratio of the sidescatter power with $\mathbf{E}_s \| \mathbf{E}_0$ to the sidescatter power with $\mathbf{E}_s \perp \mathbf{E}_0$ is 1.3 ± 0.6, still a much lower ratio than for the incident beam.

C. Plasma diagnosis

As described in Sec. II, plasma diagnosis by ruby laser holographic interferometry is performed. In a previously reported experiment,[10] the plasma was seen interferometically

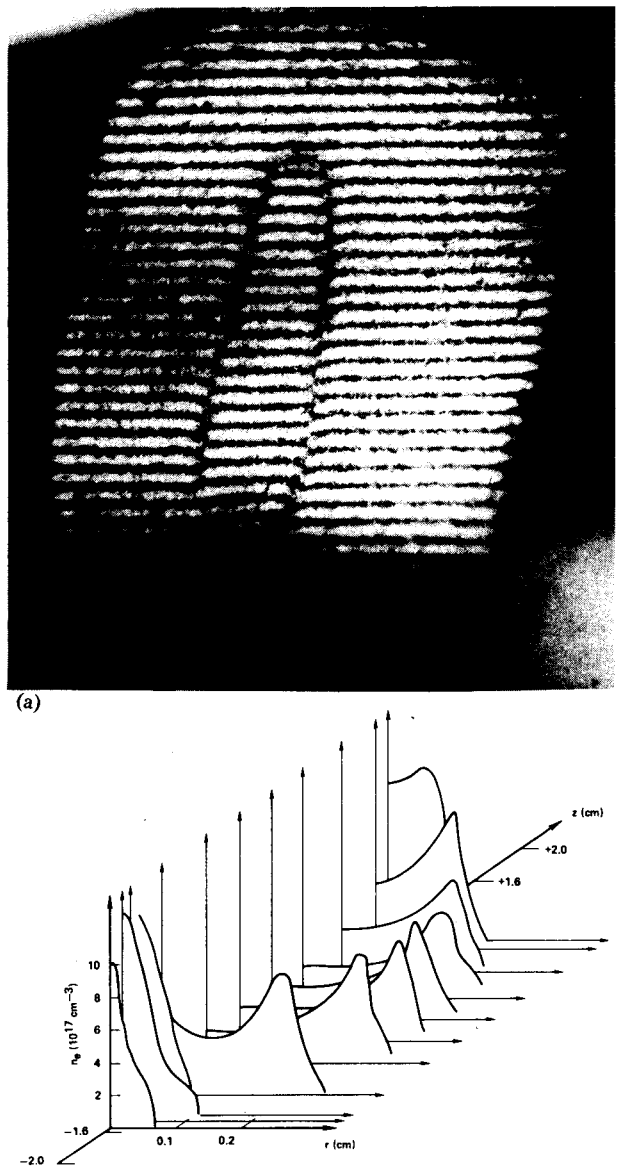

FIG. 8. (a) Ruby laser interferogram of helium plasma about 40 nsec after occurrence of sidescatter. Fringe spacing is about 900 μm, and is not finer because plasma motion during the 30-nsec FWHM ruby pulse limits resolution. The arc axis is horizontal; the CO_2 laser beam propagates from bottom to top; and the sidescatter collection axis is out of the plane of the figure. Laser-induced ionization is seen both upstream and downstream of the CO_2 focus, located at the center of the interferogram. (b) Abel inversion of the interferogram in (a), showing the density minimum on axis resulting from radial plasma exansion. The forward ionization wave seems to have momentarily stalled, since the most forward fringe already shows a density minimum on-axis. Usually, as in this case, the existence of the dense region upstream from focus is accompanied by the cessation of forward front propagation. This may well be due to a decrease in intensity downstream from the backward-moving dense front due to absorption in that region (see Ref. 10). Note that the CO_2 focus is at $z = 0$.

to evolve as a laser-supported ionization wave bleaching its way across the arc-preionized gas. Sidescatter was found to emanate from the dense plasma at the front of this disturbance; as this dense region exists within any sidescatter collection volume for only the brief period of time between laser-induced ionization and radial plasma expansion from the CO_2 axis, the short duration of observed sidescatter is easily explained.

The location of the CO_2 focal spot at the edge of the interferometric field of view in Ref. 10 prevented acquisition of any information about the plasma upstream (toward the laser) from focus. In the present experiment, the CO_2 focal spot is located centrally within the field of view, and ionization waves are seen in Fig. 8 to propagate both upstream and downstream along the input axis from that spot. Velocities of the two disturbances differ; in hydrogen, the upstream front propagates at $\simeq 1\times 10^7$ cm/sec, while the downstream wave moves at $\simeq 3\times 10^7$ cm/sec. The upstream ionization front is the faster in helium, with a velocity of $\simeq 3\times 10^7$ cm/sec; the downstream disturbance propagates at $\simeq 2\times 10^7$ cm/sec. All of these velocities have estimated errors of $\pm$ 30%. The radial velocity of plasma expansion away from the CO_2 axis behind the dense front is also determined. The measured velocities in hydrogen and helium are $(3.8 \pm 0.3)\times 10^6$ cm/sec and $(2.9 \pm 1.4)\times 10^6$ cm/sec, respectively.

As shown in Fig. 8(b), Abel inversions of the interferograms yield the on-axis electron density in the dense front. The density measured in 15.2-Torr hydrogen, where the density at full ionization is $n_e = 1.1\times 10^{18}$ cm^{-3}, is $n_e = (1.3 \pm 0.4)\times 10^{18}$ cm^{-3}. Similarly, fully ionized density and measured density in 25-Torr helium are $n_e = 1.8\times 10^{18}$ cm^{-3} and $n_e = (1.7 \pm 0.7)\times 10^{18}$ cm^{-3}, respectively. In both cases, full ionization is seen to be within the error bar of the measured value.

We have previously reported spectroscopic density measurements in hydrogen showing reasonable agreement with the interferometrically determined values.[10] In helium, measurements of the Stark-broadened linewidth of the He-II 4686-Å line yield a maximum electron density $n_e = (2.3 \pm 0.3)\times 10^{18}$ cm^{-3}, in excess of full ionization at the fill density. The line shape suggests that optical depth effects are operative, so this is considered an upper bound on electron density. From the ratio of the 4686-Å line intensity to the intensity of the continuum beneath the line, the electron temperature in the helium plasma is determined. At early times, soon after sidescatter occurs, we find $T_e = 35 \pm 5$ eV.

IV. DISCUSSION

A. Identification of sidescatter mechanisms

Six mechanisms must be considered as possible causes of the observed sidescatter: (1) stray scattered light; (2) thermal Thomson scattering; (3) stimulated Raman scattering (SRS); (4) scattering from acoustic turbulence, with Doppler shifts due to plasma mass motion; (5) dielectric reflection from the ionization wave front, with Doppler shifts due to plasma surface motion; and (6) stimulated Brillouin scattering. Stray light, scattered by vacuum system components or imperfect optics, can be eliminated because the scattered spectrum in that case would mirror the incident laser spectrum. The levels of observed sidescatter are several orders of magnitude too large to be explained by thermal Thomson scattering, and the frequency shifts are orders of magnitude too small to be explained by SRS. Mechanisms (4)–(6) will now be considered in more detail.

Plasma motion is an integral part of either mechanism (4) or (5) and can affect frequency shifts expected for (6). From the Abel-inverted interferograms, plasma motion in two directions is seen. First, after a dense plasma is created by the ionization wave at a given position along the input z axis, the plasma expands radially in the x-y plane [see Figs. 4(a) and 8(b)]. This motion does involve the plasma mass motion implicit in mechanism (4) and can also affect shifts in (6). The radial velocities reported in Sec. III C are the nearly steady-state velocities observed more than 30 nsec after the dense front begins to expand. Just after dense front formation within 20 ns of the time of observed sidescatter, evidence is found for velocities near 10^7 cm/sec. As the expansion is relatively symmetric about the input axis (as expected from momentum conservation), this would lead to a broadening of spectral features by about 20 GHz, with no net shift. This is inconsistent with our spectral observations. Features with widths much narrower than 20 GHz, which will be attributed below to SBS, are seen; apparently, this scatteing must occur before significant radial acceleration takes place. Broad features, with widths greater than 20 GHz and net shifts, are found below to be well explained by mechanism (5) with axial motion axial motion only. The effect of the radial motion on our observations seems, then, to be negligible.

In addition to the radial plasma motion, possible effects of the axial motion of the dense front must be considered. The nature of this motion is different from that of the radial expansion; it is an apparent motion, requiring no mass motion, due to the progressive ionization of the neutral particles just ahead of the front. In other words, it is due to the propagation of an ionization disturbance through the plasma, rather than due to the motion of the plasma itself. As such, it cannot affect any volume scattering mechanisms such as (4) or (6). However, the surfaces defining the dense front do move along the input axis, and reflections due to the discontinuities in dielectric constant at these interfaces will experience the Doppler frequency shifts of mechanism (5).

To assess the importance of this mechanism in explaining our hydrogen sidescatter observations, a simple experiment is performed. Since an ionization front is seen to propagate in each direction away from focus, the Doppler shift expected from surface motion will change sign as the collection volume is moved through focus along the input axis. Downstream from focus, a red shift due to the forward-propagating disturbance will be seen; but upstream from focus, a blue shift is expected from the backward-moving front. Indeed, as our sidescatter collection volume is moved through focus, a shift in the weight of the hydrogen sidescatter spectrum is seen. Downstream from focus, the blue end of the spectrum vanishes, suggesting that this is due to the backward ionization wave. On the other side of focus, however, a broad spectrum is seen with a red component still present,

though reduced from that observed in focus [Fig. 4(c)]. This suggests that not all of the red-shifted sidescatter is due to Doppler shift from the forward moving surface. The width of the broad spectrum observed in hydrogen at both $\phi = 0°$ and $\phi = 90°$ correlates with Doppler shifts due to the axial velocities quoted in Sec. III C, as do the relative magnitudes of the red and blue shifts. For these reasons, we feel that the dielectric reflection mechanism explains all of the blue-shifted sidescatter and part of the red-shifted sidescatter in hydrogen. This sidescatter can well be isotropic and depolarized as observed if the reflecting surface has roughness of scale comparable to the incident wavelength.[11]

The portion of the hydrogen sidescatter not explained by the dielectric reflection mechanism is always red shifted, as mentioned above. Coupled with the fact that a portion of the red-shifted sidescatter shows the anisotropy expected for SBS, and with the apparent slow growth of sidescatter reflectivity with input power, we feel that SBS sidescatter is the most likely mechanism responsible for this additional sidescatter. The evidence is circumstantial, however.

In helium, a much clearer case for the dichotomy suggested in hydrogen can be made. Two kinds of sidescatter, with distinct time histories (Fig. 5), spectra (Fig. 6), and growth curves (Fig. 7) are observed. Multiple-spike sidescatter exhibits the broad spectrum one might expect, by analogy with our hydrogen interpretation, for dielectric reflection from the moving ionization fronts. As in hydrogen, a comparison with the velocities of those waves shows reasonable agreement between the observed spectrum and that expected from forward and backward Doppler shifts. Again, as with hydrogen, this sidescatter shows isotropy in the plane orthogonal to the incident wave vector and is depolarized. The sidescatter power depends linearly on incident power (reflectivity, the ratio between scattered and incident powers, is constant). For all of the above reasons, dielectric reflection is deemed the most likely mechanism for multiple-spike sidescatter.

On the other hand, the single-spike sidescatter shows almost all of the expected properties of SBS. A red shift from the incident spectrum is seen in Fig. 6(a), and a definite increase of reflectivity with incident power is observed in Fig. 7. Since all of the sidescatter at $\phi = 0°$ has the spectrum and growth characteristic of the dielectric reflection mechanism, sidescatter having the growth and spectrum expected for SBS also has the required anisotropy because it does not occur at $\phi = 0°$.

The one property of single-spike sidescatter which is inconsistent with SBS is the polarization of the scattered light; SBS growth should lead to linearly polarized scattered light. However, a reasonable explanation can be made using backscatter data as follows. Because identification of SBS backscatter in Ref. 2 was felt to be conclusive, an experimental test of the polarization of the scattered light was undertaken. It was found that at the highest levels of backscatter observed at saturation (see Fig. 3 of Ref. 2), scattered light was linearly polarized with the same polarization as the input beam. Along the growth region of the curve, however, significant depolarization from that of the input was observed, the degree of depolarization increasing as lower levels of backscatter were examined. This suggests that the SBS backscatter grows from an unpolarized noise source, with growth by orders of magnitude above that level being required to see linear polarization of the scattered light. To see whether the dielectric reflection mechanism could provide such an unpolarized noise source, backscatter due to this process was purposely induced by raising the fill presure of the hydrogen gas above critical density. The resulting blue-shifted (from a backward-moving ionization front) backreflection was indeed found to be depolarized.

Since the single-spike sidescatter has not grown as far above the noise level as the backscatter in Ref. 2, it is perhaps not surprising that the scattered light is still depolarized. As all of the other sidescatter properties are consistent with SBS, this sidescatter is attributed to the SBS mechanism.

B. Analysis of Brillouin sidescatter

Having identified stimulated Brillouin sidescatter, as described above, we now wish to extract as much information about growth rates, noise sources, and saturation mechanisms as our data allow. Before embarking upon this discussion, we must estimate one parameter upon which our discussion will depend, and which cannot be measured directly in this experiment—T_e/T_i. To do this we make use of two independent relations containing T_e and T_i and solve for these temperatures and, therefore, for their ratio. The first such relation is simply the ion acoustic dispersion relation, into which we insert the measured SBS sidescatter frequency shift[12]:

$$\Delta\nu_{\mathrm{SBS}} = k_{\mathrm{ac}} v_{\mathrm{ac}}/2\pi = (2\pi)^{-1}(2k_0 \cos 45°) \times [(ZT_e + 3T_i)/M]^{1/2}, \tag{1}$$

where Z and M are the ion charge and mass, respectively, and where $\gamma_i = 3$ has been assumed. The second relation is the definition[13] of electron-ion equilibration time τ_{ei}:

$$dT_i/dt = (T_e - T_i)/\tau_{\mathrm{eq}}. \tag{2}$$

where τ_{eq} is sensitive to T_e. By dimensional analysis of Eq. (2), we arrive at

$$T_e/T_i \simeq 1 + [\tau_{\mathrm{eq}}(T_e)/\Delta t], \tag{3}$$

where Δt is the time available for ion heating by laser-heated electrons. For our case, this time is taken to be 7.5 nsec from measurements of laser pulse shape and time evolution of n_e and T_e. Solving Eqs. (1) and (3) simultaneously yields $T_e \simeq 75$ eV and $T_e/T_i \simeq 4$ in hydrogen, and $T_e \simeq 33$ eV and $T_e/T_i \simeq 1.5$ in helium. By comparison, the spectroscopic result of Sec. III C for helium is $T_e = 35 \pm 5$ eV, thus lending credence to the correctness of this model.

In order to compare the sidescatter versus input intensity growth curve with theory, we must establish whether or not inhomogeneities are important. From the Abel inversion of interferograms showing the dense front, we find relatively gentle radial density gradients in both hydrogen and helium with $L_n = n(dn/dr)^{-1} \geqslant 500\,\mu$m within the focal spot radius of $140 \pm 15\,\mu$m. One theoretical treatment[14] of the inhomogeneous (linear mismatch) case including wave damping indicates that, if this were the dominant inhomogeneity, the finite-length homogeneous growth rate should be seen in our

case. The scale length of the radial temperature profile is not measured; insufficient spectral line emission intensity precludes spatial resolution of the temperature measurement described in Sec. III C. However, the above-mentioned theoretical treatment indicates that, for $L_T = T(dT/dr)^{-1} \geqslant 500$ μm, finite-length homogeneous theory should again be a good approximation. Assuming that temperature gradient scale lengths are at least as long as density gradient scale lengths, we use the homogeneous theory.

Taking (1) the CO_2 intensity measured in vacuum (neglecting self-focussing), (2) the electron density and ion charge corresponding to the full ionization inferred from the diagnostics, and (3) the electron temperature and electron-ion temperature ratio as described above, one may infer the interaction length from the slope of the SBS growth curve, as described in Ref. 2. In hydrogen, the large error bars in Fig. 3 lead to a rather inconclusive $L = 300 \pm 300\,\mu$m. The helium growth curve, on the other hand, yields $L = 210 \pm 50\,\mu$m. This is comparable to the measured full width at half maximum of our laser focal spot, $d_f = 280 \pm 30\,\mu$m, and therefore tends to support the assumption that inhomogeneities can be neglected.

As in Ref. 2, we can extrapolate the growth curves (Figs. 3 and 7) back to zero input power to infer the noise level from which the Brillouin sidescatter grows. In helium, one sees that the levels of the multiple-spike and single-spike sidescatter merge at zero input power. This suggests that the noise source from which the SBS grows is the dielectric reflection from the moving ionization fronts. We may infer the same in hydrogen; there, due to its slower growth, the SBS sidescatter appears from the spectra in Fig. 4 to have just grown above the dielectric reflection level.

In the light of our sidescatter measurements, perhaps a more definite statement about the noise source for our SBS backscatter (Ref. 2) should be made. The noise reflectivity per unit solid angle extrapolated in Fig. 3 appears to be in agreement with the noise level inferred from the backscatter growth. The dielectric reflections from the ionization fronts may well be seeding the growth of backscatter in the long interaction region behind the front. Measurements of backscatter polarization discussed in Sec. IV A of the present work, which indicate growth from an unpolarized noise source, support such a hypothesis.

Finally, we can investigate the saturation level of the sidescatter in helium and compare with possible saturation mechanisms. Unfortunately, the ion density fluctuation level in the dense front, where sidescatter occurs, is not easily inferred from the sidescatter level. In Ref. 2, masking portions of the input beam showed that the backscattered light was highly directional, with much less scattered light at nearby angles. The scattering source, therefore, was nearly a single wave whose density fluctuation level was correctly inferred from the Bragg scattering relation. The sidescatter does not show such directionality. Given our spot size, the diffraction maximum of scattered light from a single wave would have a full width at half maximum of less than 2°; sidescattered light, on the other hand, is found to fill the 10° cone of our collection lens relatively uniformly. This indicates that waves of comparable amplitude are propagating in at least a 5° cone near the 45° ion acoustic wave responsible for 90° scattering. We have no reason to doubt that waves in a much wider range of angles are propagating.

Ideally, then, one would have to measure scattered power at all angles in order to infer the density fluctuation level in the dense front. We propose, however, that a reasonable estimate may be made from two calculations. First, if we assume that the scattering that we see is most of the light scattered by the dense front (which is equivalent to assuming that the 45° ion wave dominates the density fluctuation level in that region), we can obtain a lower bound on the fluctuation level. The Bragg relation for 90° scattering is[15]

$$P_s/P_i = (1/6\pi) r_0^2 \lambda_0^2 \tilde{n}^2 L_z d_f, \tag{4}$$

where $r_0 = e^2/mc^2$ is the classical electron radius, λ_0 is the incident wavelength, $\tilde{n}$ is the 45° ion wave amplitude, L_z is the interaction length along the input axis, and d_f is the focal spot diameter. We find for our parameters that this implies $\tilde{n}/n \simeq 0.1\%$.

A second calculation may be used to yield a likely upper bound on the density fluctuation level. The dimensions of our dense front along the input axis and across the focus are comparable, resulting in very little difference between interaction lengths for ion wave growth at various angles within the front. As the SBS growth rate is insensitive to θ (though not to ϕ!) for small $k\lambda_D$, one expects that ion waves will be driven in a wide range of angles inside the dense front, leading to scattering at a wide range of angles. Hence, as the ion waves saturate at comparable density fluctuation levels, the scattered reflectivity (proportional to $\tilde{n}^2 L^2$) should be comparable. If we assume that the scattered power density we see at $\theta = 90°, \phi = 90°$ appears in all 4π of solid angle around the dense front, we probably do not significantly understimate contributions from any θ near $\phi = 90°$, but we certainly overestimate contributions from solid angles near $\phi = 0°$, where SBS sidescatter is not seen. Unless there exists a significant fraction of solid angle where the scattered level per unit solid angle is much higher than we see in our collection angle, so as to more than make up for our overestimate of scatter from angles near $\phi = 0°$, we have a likely overestimate of the density fluctuation level. The 5% backscatter reflectivity, it should be remembered, does not reflect upon the density fluctuation level in the dense front, since this large level is due to amplification in the long region behind the dense front.[10] Only the noise level for backscatter is believed to emanate from the dense front, as discussed above, and this has comparable reflectivity per steradian to that of sidescatter. It should be noted from Eq. (4) that if our assumption is not correct, $\tilde{n}/n$ will scale only as the square root of the average scattered power per unit solid angle. With this assumption of isotropic ion waves, we find $\tilde{n}/n \simeq 1\%$.

Having found that the density fluctuation level at saturation is likely to be in the 0.1–1.0% range, we may compare this with the levels expected from various saturation mechanisms. As in Ref. 2, we find that pump depletion, wave breaking, energy and momentum deposition, electron heating, and ion heating should not limit the reflectivity or density fluctuation to such a low level. A theoretical prediction[16] for limitation of wave amplitude by harmonic generation at

$\tilde{n}/n = k^2\lambda_D^2$ ($\simeq 0.2\%$ in this case) is not consistent with experimental observations of ion waves in filament-discharge plasmas.[17] In previous work[2] we found that ion trapping was the most likely mechanism that would lead to the low levels of backscatter observed. This is also the case here with sidescatter. However, instead of the waterbag model[16] for trapping, we now use a more detailed theory which does not require the absence of particles with $v \simeq c_s$. Ikezi *et al.*[18] have shown, in experiment and theory, that ion trapping causes a negative frequency shift $\Delta\omega$ and a positive shift in wavenumber Δk, and thus a decrease in wave velocity. These shifts are caused by the need to conserve energy and momentum in the wave frame when particles are trapped.[19] The effect of the decrease in phase velocity ω/k is to greatly increase ion Landau damping, and thus to inhibit the further growth of the wave. The change in ω/k is given by[18]

$$\Delta\left(\frac{\omega}{kc_s}\right) \simeq \frac{\Delta\omega}{\omega} - \frac{\Delta k}{k} = 2\frac{\Delta\omega}{\omega} \simeq -2c_s^3(\partial^2 f_0/\partial v^2)_{v=c_s}|\tilde{n}/n|^{1/2}, \tag{5}$$

where $f_0(v)$ is the normalized, one-dimensional Maxwellian distribution. As a rough estimate, we may set this equal to the half-width of the SBS growth curve.[20] For $zT_e/T_i = 3$, this is[20] $\Delta(\omega/kc_s) \simeq 0.26$, which yields $|\tilde{n}/n| \simeq 0.8\%$. This estimate agrees with the order of magnitude deduced from the sidescatter level.

V. CONCLUSIONS

A number of conclusions may be drawn from the present work and from comparisons of these measurements with those of Ref. 2. First, we are able to attribute the sidescatter from our laser-altered preionized gas to two mechanisms, SBS and dielectric reflection. This constitutes the first reported identification of stimulated Brillouin sidescatter from a laboratory plasma. The growth rate of the SBS sidescatter agrees, within the framework of our stated assumptions, with the theoretical growth rate in a finite-length homogeneous plasma. More importantly, given our assumptions, the saturation level of this sidescatter agrees best with the same saturation mechanism proposed for SBS backscatter in Ref. 2.

If the same ion wave nonlinearities lead to saturation of sidescatter and backscatter, one can make a statement concerning the expected relative levels of the two. At least as long as the interaction is not dominated by inhomogeneities, the reflectivities will scale as $(\tilde{n}L)^2$. With $\tilde{n}$ limited similarly, one can expect relative levels of sidescatter and backscatter to depend on the relative magnitude of the interaction lengths for the two. In our experiment, a much longer growth region is available for backscatter than for sidescatter, leading to the large discrepancy between the hydrogen backscatter level in Ref. 2 and the hydrogen sidescatter level in the present work. In solid target experiments, it is quite possible for the interaction lengths in the two directions to be comparable, leading to similar levels of sidescatter and backscatter. Such a result has, in fact, been obtained in a recent experimental study of sidescatter and backscatter from solid targets.[7] In that study, isotropic sidescatter was observed with small interaction length, but anisotropic sidescatter was seen if the interaction length was increased at the same intensity. Backscatter and total sidescatter were found to be comparable in the latter case.

Two statements may be made about the importance of the second sidescatter mechanism, dielectric reflection. First, it would appear that this is the likely noise source from which both SBS sidescatter and backscatter are growing, as explained in Sec. IV. Secondly, as this sidescatter is isotropic and depolarized, it may well be the mechanism responsible for the depolarized,[17] isotropic[3-9] sidescatter that has often been referred to as "diffuse scatter" in solid target experiments.

ACKNOWLEDGMENTS

We have benefited from conversations with R. P. Godwin, N. C. Luhmann, Jr., C. Surko, and others. We would also like to thank Mr. Ken Marsh and Dr. Akio Yasuda for assistance in data acquisition during portions of the experimental work. This work was supported by the U.S. Department of Energy, Contract EY-76-S-03-0034, P.A. 236; Los Alamos Scientific Laboratory, P. O. No. 4-X49-0027K; and the National Science Foundation, Grants 75-16610 and 77-17861.

[1] J. F. Drake, P. K. Kaw, Y. C. Lee, G. Schmidt, C. S. Liu, and M. N. Rosenbluth, Phys. Fluids **17**, 778 (1974).
[2] M. J. Herbst, C. E. Clayton, and F. F. Chen, Phys. Rev. Lett. **43**, 1591 (1979), and references contained therein.
[3] R. A. Haas, H. D. Shay, W. L. Kruer, M. J. Boyle, D. W. Phillion, F. Rainer, V. C. Rupert, and H. N. Kornblum, Phys. Rev. Lett. **39**, 1533 (1977).
[4] R. A. Haas, W. C. Mead, W. L. Kruer, D. W. Phillion, H. N. Kornblum, J. D. Lindl, D. MacQuigg, V. C. Rupert, and K. G. Tirsell, Phys. Fluids **20**, 322 (1977).
[5] B. H. Ripin, Appl. Phys. Lett. **30**, 134 (1977).
[6] B. H. Ripin, F. C. Young, J. A. Stamper, C. M. Armstrong, R. DeCoste, E. A. McLean, and S. E. Bodner, Phys. Rev. Lett. **39**, 611 (1977).
[7] M. D. Rosen, D. W. Phillion, V. C. Rupert, W. C. Mead, W. L. Kruer, J. J. Thomson, H. N. Kornblum, V. W. Slivinsky, G. J. Caporaso, M. J. Boyle, and K. G. Tirsell, Phys. Fluids **22**, 2020 (1979).
[8] B. Grek, H. Pepin, T. W. Johnston, J. N. LeBoeuf, and H. A. Baldis, Nucl. Fusion **17**, 1165 (1977).
[9] K. Eidmann, G. Brederlow, R. Brodmann, R. Petsch, R. Sigel, G. Tsakiris, R. Volk, and S. Witkowski, Max-Plank Institute, Garching, Germany, Report PLF 15 (1979).
[10] M. J. Herbst, C. E. Clayton, W. A. Peebles, and F. F. Chen, Phys. Fluids **23**, 1319 (1980).
[11] P. Beckmann and A. Spizzichino, *The Scattering of Electromagnetic Waves from Rough Surfaces* (Pergamon, Oxford, 1963).
[12] As described in Ref. 2, the exact kinetic treatment involves finding the frequency at which $\mathrm{Im}[\chi_e(1+\chi_i)/(1+\chi_e+\chi_i)]$ maximizes, where χ_e and χ_i are the electron and ion susceptibilities. Equation (1) is a good approximation to this, even at our low T_e/T_i.
[13] L. Spitzer, Jr., *Physics of Fully Ionized Gases*, 2nd ed. (Interscience, New York, 1962), p. 135.
[14] D. Pesme, G. Laval, and R. Pellat, Phys. Rev. Lett. **31**, 203 (1973).
[15] L. D. Landau and E. M. Lifshitz, *Electrodynamics of Continuous Media* (Pergamon, New York, 1960).
[16] J. M. Dawson, W. L. Kruer, and B. Rosen, in *Dynamics of Ionized Gases*, edited by M. Lighthill, I. Imai, and H. Sato (Univ. of Tokyo Press, Tokyo, 1973), pp. 47–61.
[17] N. C. Luhmann, Jr. and W. A. Peebles (private communication).
[18] H. Ikezi, K. Schwarzenegger, A. L. Simons, Y. Ohsawa, and T. Kamimura, Phys. Fluids **21**, 239 (1978).
[19] G. J. Morales and T. M. O'Neil, Phys. Rev. Lett. **28**, 417 (1972).
[20] M. J. Herbst, Thesis, UCLA PPG-382 (1979).
[21] D. W. Phillion, R. A. Lerche, V. C. Rupert, R. A. Haas, and M. J. Boyle, Phys. Fluids **20**, 1892 (1977).